INSTITUTE OF PLASMA PHYSICS

NAGOYA UNIVERSITY

AMOUNT OF IMPURITY AND ITS BEHAVIOR IN THE STP-2 SCREW PINCH TOKAMAK

S. Yamaguchi
(Received - Mar. 27, 1981)

IPPJ- 517 May 1981

RESEARCH REPORT

NAGOYA, JAPAN

AMOUNT OF IMPURITY AND ITS BEHAVIOR IN THE STP-2 SCREW PINCH TOKAMAK

S. Yamaguchi
(Received - Mar. 27, 1981)

IPPJ- 517 May 1981

Further communication about this report is to be sent to the Research Information Center, Institute of Plasma Physics, Nagoya University, Nagoya 464, Japan.

ABSTRACT

Temporal and spatial evolution of oxygen spectral line intensities have been measured in the STP-2 screw pinch tokamak. The electron density and temperature as measured by Thomson scattering are of the order of 10^{14} cm^{-3} and 10 eV, respectively. On the basis of these measurements, quasi-steady-state rate equations have been solved to give the OII and OIII ion densities. It is found that the density of oxygen impurity is about several percent of the electron density, and the impurity moves with the bulk plasma. It is confirmed that the impurity originates from the wall of the discharge tube during the initial phase of the discharge.

1. INTRODUCTION

Despite many efforts to achieve good confinement of high beta plasmas in toroidal pinch devices [1-3], both the electron temperature T_e and the energy confinement time τ_e reported so far are only of the order of 30 eV and 50 μsec, respectively, and remain quite unsatisfactory when compared with those obtained in tokamak devices. Furthermore the scaling law has not yet been established for the toroidal pinch geometry. As for the origin of the above difficulty two points are commonly noted; the first is the MHD-instability and the second is the impurity problem.

It is difficult to obtain a stable MHD-configuration for a high beta plasma [4,5]. In the STP-2',for example, when operated in a high beta mode, strong instabilities take place and the plasma column is destroyed completely [6]; in this case plasma confinement is limited by the instabilities. Impurity, on the other hand, is also important in confining a high density plasma. If we want to have a more stable plasma in the STP-2, we choose a weak pinch mode; as a result of this the highest T_e is as low as 20 eV just after the shock heating. The radiation loss rate coefficient $C(T_e)$ by light impurity is large for such a low temperature: e.g., for oxygen it is estimated to be $\simeq 8 \times 10^{-26}$ W cm^3 [7]. The radiation power loss P_r is given as

$$P_r = C(T_e) \cdot n_{imp} \cdot n_e \quad (W \cdot cm^{-3}) \quad , \qquad (1)$$

where n_{imp} and n_e are impurity and electron densities. The electron density usually obtained in pinch devices is about 10^2 times as large as those in tokamaks. Therefore, if the impurity ratio n_{imp}/n_e were

the same order as in tokamak plasmas, the radiation power loss would be higher by more than four orders of magnitude, and it would become the major loss mechanism in the energy balance of pinch plasmas. It is noted by the computer simulation [8] that the ratio n_{imp}/n_e should be less than 1 % for oxygen impurity in order to obtain appreciable subsequent heating for a pinch plasma with $T_e \simeq 10$ eV and $n_e \simeq 10^{14}$ cm^{-3}. From this standpoint, it is essential to know the amount of impurities present in a pinch plasma.

In order to understand the dynamics of the plasma, the origin as well as the temporal-spatial behaviors of the impurities are also important. For instance, computer simulations sometimes assume that the concentration of impurities is proportional to n_e and has the similar temporal-spatial behavior to that of the bulk plasma. Such an assumption should be examined experimentally.

In Sec.2 the discharge condition and experimental technique are described in the present experiment. Sec.3 are divided into three sub-sections; in Sec.3.1 plasma parameters and line intensities of oxygen are given along with qualitative consideration of the ionization state of impurity, the ion densities of OII and OIII are calculated in Sec.3.2 and the origin and the temporal-spatial behaviors of impurities are discussed in Sec.3.3. The discussion and conclusion are given in Sec.4.

2. DISCHARGE CONDITION AND EXPERIMENTAL TECHNIQUE

Figure 1 shows the STP-2 [9] and the positions of the diagnostics apparatus around the torus. The major and minor radii of the quartz discharge tube are 25 and 9.5 cm, respectively. The working deuterium gas was puff-injected into the torus and the number density was 3.5 x

10^{14} cm^{-3}. Preionization was accomplished by using a small coaxial plasma gun followed by a relatively weak Z-discharge under the weak toroidal field; the degree of ionization achieved was 5 to 10 %. The maximum main plasma current I_p and toroidal field B_t were 30 kA and 9.2 kG. Representative waveforms are shown in Fig.2. The safety factor was nearly 5 at the wall, and the toroidal beta became almost 1 % at the center of the plasma while poloidal beta exceeded about 2 on the edge of the main plasma. These parameters were chosen so as to obtain relatively smooth motion of the plasma. The lifetime of the plasma is about 25 μsec and is restricted by the external circuits.

Figure 3 shows a schematic drawing of the spectroscopic measurement system. The monochromator has following characteristics; the focal length is 20 cm, the resolution 10 Å and slit height 10 mm. All of the optical components (lenses, optical fiber and window of the photomultiplier) are made of quartz. The observation solid angle is 10^{-4} str and is determined by a small lens with a diameter of 8.0 mm attached to the inlet end of the fiber. The inlet of the fiber is placed on the plastic rail that is attached to the toroidal coils at a point 20 cm above the equatorial plane of the torus; the discharge tube bore 19 cm in diameter can be scanned with the fiber over a distance of 13.5 cm; the observation points are seven and the spatial resolution of the system is about 2 cm at the mid plane of the torus. The outlet has a rectangular cross section 10 mm high and 1 mm wide. The outside of the discharge tube are painted black so as to avoid stray light reflected from the discharge tube wall. An NBS standard tungsten lump is used for absolute intensity calibration.

The electron density and temperature were measured by the laser scattering system placed at the angle $\phi = 180°$ from the spectroscopic

system. The laser system was calibrated by Rayleigh scattering from nitrogen gas. The CO_2 laser interferometer system at $\phi = 90°$ was also used to confirm the density measurement of the laser scattering.

The data processing system [10] for the spectroscopic measurement has been developed; the observed spatial profile of the line intensity is converted to the emission coefficient as a function of tube radius. The line intensity profile is drawn by using the cubic natural spline function [11] that connects average values of several shots. In the STP-2, however, cylindrical symmetry can not be assumed because of high beta effects of the plasma; the center of the plasma deviates from the axis of the discharge tube and the shape of the plasma cross section is not always circular. Therefore, it is necessary to use the cylindrically asymmetric Abel inversion [12]. In this method all of the data of the line intensities are divided into two parts; asymmetric odd part and symmetric even part with respect to the center of the discharge tube. The symmetric part is inverted by the Barr's method [13] and the asymmetric part is fitted on the odd function that modified cylindrical symmetry. The assumption of symmetry is retained for the direction of observation. It has been found that the error in the emission coefficient can be assumed to be the same order as that for line intensity itself, and it is about 20 to 30 % in the present case where the accuracy is limited by the outside values of the line intensity.

3. EXPERIMENTAL RESULT AND ANALYSIS

3.1 Time History of Plasma Parameters and Impurity

The spatial profiles of the electron density and temperature measured at 5 μsec are shown in Fig.4. The error bar of these values has

been estimated by using the least square fitting method and the spatial error bar corresponds to the slit height of the monochromator used in Thomson scattering measurement. The temporal evolution of the spatial profile of the electron density is also shown in Fig.5 for ≥ 4 μsec.

Figure 6 indicates the time history of the electron density and temperature at the center of the discharge tube. The electron density increases for ≤ 8 μsec. It decreases after 8 μsec while the spatial integration of the electron density over the discharge tube does not change appreciably because the plasma column moves toward inner part of the tube as depicted in Fig.5. On the other hand, the electron temperature increases rapidly at the initial phase to reach the peak in 3 μsec, and it decreases rapidly after 3 μsec. This rapid decrease in the electron temperature means that the energy confinement time τ_e is very short and about 5 μsec.

This value is almost 10^2 times as small as the estimated one applying the tokamak scaling law [14] to the parameters of the STP-2. Such a short τ_e is one of the most serious problems in pinch devices, and the short τ_e might be the radiation and ionization losses of light impurities.

The temporal evolution of the line intensities of oxygen is shown in Fig.7 that is observed at the center of the discharge tube, where numbers 1, 2 and 3 indicate the lines of OI, OII and OIII, respectively. An OIV line was observed but it was blended with a line of OII; the peak time was found to coincide approximately with that of OII. As is seen in Fig.7, the peak time of the higher ionized-ion line is later compared with that of lower ionized-ion. This fact suggests that ionization proceeds stepwise until 6 μsec.

Figure 8 shows the ionization potential and the estimated ioniza-

tion time τ_o for oxygen ions. The τ_o is defined by

$$\tau_o = \frac{1}{n_e \cdot S_{i \to j}} \quad \text{(sec)} , \tag{2}$$

where $S_{i \to j}$ is the ionization rate coefficient from ion i to j. The semi-empirical formula by Lotz [15] has been adopted to give τ_o for the plasma with T_e = 10 eV and $n_e = 10^{15}$ cm^{-3}. It should be noted, however, that this formula accounts for only the direct ionization and we neglect the contribution from the ionization via excited levels [16,17]. Our STP-2 plasma has the electron density of the order of 10^{14} cm^{-3} in Fig.5, so that the latter contribution should be included. As a rough estimate, the effective ionization potential has been reduced according to ref.[17] and the effective ionization time τ^* has been estimated (Fig.8). This has not been done for OIV ion because this has very long ionization time compared with the lifetime of the plasma. It is suggested from Fig.8 that almost all oxygen ions are ionized to OII within 2 μsec or less after the start of the main discharge. In the next 1 to 2 μsec, with as increase in n_e, OII ions are ionized to OIII ions completely. From these considerations it is assumed that almost all oxygen ions are in the state of OIII after 4 μsec and the population densities of OII and OIV are small.

The plasma is considered to be in the ionizing-state for OII and OIII before 6 μsec and the recombination is not included in Fig.8. For the later times than 8 μsec the recombination is not negligible for OIII because the electron temperature is about 5 eV all over the plasma column. However, it is well assumed that OIII ions are still dominant even after 8 μsec because the recombination time is long [17].

3.2 Population Density of Oxygen Impurity

The quasi-steady-state analysis has been performed at 5 μsec, where the temporal and spatial variations of T_e and n_e are rather smooth and oxygen is well assumed to be in the ionizing-state [16]. Rate equations for excited states are solved in order to obtain the ground state population density of the impurity ion. Spatial profile of the line intensity of OIII (3760 Å; $2p3s(^3P^0)$ - $2p3p(^3D)$) has been measured and the population density of $2p3p(^3D)$ was calcualted by using the asymmetric Abel inversion. Figure 9 shows the density profile of OIII ($2p3p(^3D)$) at 5 μsec. The error of the density is about 20 to 30 % because the typical scattered error of observed line intensity is also 20 %. Figure 10 shows the partial energy level diagram of OIII in the triplet series. OIII ion has the singlet and quintet series and the ground state of OIII is $2s^22p^2(^3P)$. The rate equations are considered for the states of $2p3p(^3D)$ and $2p3s(^3P^0)$. As the plasma is in the ionizing-state for OIII ions, the recombination from OIV ion and de-excitations higher lying are not neglected. The populating and de-populating mechanisms considered for these states are shown in Fig.10. The solid lines mean excitation, de-excitation and ionization by electron impact and the wavy lines mean radiative transition. The populating mechanisms from $2s2p^3$ to 2p3s and 2p3p are neglected because these processes are two electron transitions, and the cross sections between those states are well expected to be very small. According to the method of the quasi-steady-state solution [18-20], the time derivative of the excited-state population density is approximated to zero. From these considerations, the rate equations for the states of $2p3s(^3P^0)$ and $2p3p(^3D)$ are

$$n_e \cdot n_{2p} \cdot C_{2p\to3p} + n_e \cdot n_{3s} \cdot C_{3s\to3p} - n_{3p}\{A_{3p\to3s}$$

$$+ n_e(F_{3p\to3s} + F_{3p\to2p} + C_{3p\to3d} + S(3p))\} = 0 \ , \qquad (3)$$

$$n_e \cdot n_{2p} \cdot C_{2p\to3s} + n_{3p}(A_{3p\to3s} + n_e F_{3p\to3s})$$

$$- n_{3s} \cdot \{A_{3s\to2p} + n_e(F_{3s\to2p} + C_{3s\to3p} + S(3s))\} = 0 \ , \qquad (4)$$

where n_{2p}, n_{3s} and n_{3p} are the population densities of the ground state, 2p3s($^3P^0$) and 2p3p(^3D), respectively. Other notations in Eqs.(3) and (4) are following:

$C_{i\to j}$: rate coefficient for excitation from level i to j by electronic collision [21],

$F_{j\to i}$: rate coefficient for de-excitation from level j to i, and is equal to $C_{i\to j}(\omega_i/\omega_j)\exp(E_{ij}/T_e)$,

$S(i)$: rate coefficient for ionization from level i to OIV ion [15],

$A_{j\to i}$: Einstein coeffcient for radiative transition from level j to i [22],

ω_i : statistical weight of level i,

E_{ij} : excitation energy from level i to j.

The unknown densities n_{2p} and n_{3s} have been obtained by employing the measured electron density and temperature in Fig.4, and the population density of 2p3p(^3D) in Fig.9. Figure 11 shows the result of the calculation. The dotted line indicates the population density profile of $2s^22p^2(^3P)$. As mentioned above OIII ion has singlet and quintet series other than triplet. Since the collisional cross sections between these states are large [23] and the transition probabilities are small

because of forbidden transitions, these states may be thermalized. The excitation time τ_{exc} is defined by

$$\tau_{exc} = \frac{1}{n_e \cdot C_{exc}} \quad (\text{sec}) , \qquad (5)$$

where C_{exc} is the excitation rate coefficient [23]. The value of τ_{exc} is about 0.5 μsec when T_e and n_e are 10 eV and 10^{15} cm^{-3}, respectively. In fact, it is pointed out in ref.[24] that $2s2p^3(^1D, ^5S)$ are thermally populated against $2s^22p^2(^3P^0)$ under the condition of $n_e \geqq 10^{10}$ cm^{-3}. Therefore, the population densities of quintet and singlet levels have been included and in Fig.11 the solid line shows the sum of the population densities of singlet, triplet and quintet levels.

In above calculation the largest error may arise from the uncertainty of the rate coefficient $C_{2p \to 3p}$. This transition is forbidden and the excitation cross section or the oscillator strength is not available from literature, so that the following estimate has been done. We consider the excitation cross sections of 2p→3s, 2p→3p and 2p→3d for hydrogen atom from ref.(25), and calculate the rate coefficeints of these transitions. The rate coefficients of 2p→3s and 2p→3d for OIII are estimated from the empirical formula [21] with the oscillator strengths [22]. Using the scaling law for Z-charged ion [26], the ratio between the rate coefficients of 2p→3s and 2p→3d for II is found to be nearly equal to that of hydrogen. Consequently, it is assumed that the ratios of the rate coefficients of 2p→3d to 2p→3p for hydrogen atom and OIII ion are equal each other. There are other type of errors arising from the errors of the measured electron density, temperature and the population density of $2p3p(^3D)$. The dependence of the ground state density is examined on these quantities and found to be proportional to n_{3p} and

$\sqrt{n_e}$ roughly. When electron temperatures vary by 1 eV around 10 eV, the variation of $\delta n_{2p}/n_{2p}$ is about 25 %. The assumption that the ground states of different series are thermalized may become invalid in the low electron density region, and in Fig.11 the actual density profile may overestimate in the outer region. Consequently, the total error in Fig.11 is estimated to be less than a factor of 4.

A similar analysis has been carried out for OII ion. The line intensity profile of OII (4076 Å; $2p^2 3p(^4D^0)$ - $2p^2 3d(^4F)$) has been measured and the population density of OII ($2p^2 3d(^4F)$) was obtained by the Abel inversion in Fig.9. The quasi-steady-state rate equations have been considered for the states of $2p^2 3s(^4P)$, $2p^2 3p(^4D^0)$ and $2p^2 3d(^4F)$ on the ionizing-plasma assumption. The ground state density at 5 μsec was obtained and shown in Fig.12. Similar discussions for the error also applies to OII ion. In this case, however, the ionization potential of OII is small compared with that of OIII, and the error due to an uncertainty of the electron temperatures becomes less severe: the relative variation of the ground state density is within 10 % for a change of 1 eV around 10 eV. The total error in the ground state population density of OII becomes smaller and a factor 4 is also enough in Fig.12.

The density profile of OII is hollow-like and its density radius is larger than that of OIII. This is because the electron temperature and density are enough high to ionize OII ions in the central part of the plasma. The relative ion density of OII is about $10^{-1.5}$ times as large as that of OIII.

A similar analysis has been also carried out for OIV ion at 5 μsec. Although the observed OIV line was blended with that of OII, the upper found of ground state population density of OIV has been calculated

under the assumption that all of the line intensity comes from OIV. Then the calculated population density was of the order of 10^{13} cm^{-3} or less. From the above discussions it is concluded that OIII ions are dominant compared with other ionized stage of oxygen. This conclusion is in consistent with the discussion in Sec.3.1. The total amount of the oxygen impurity in the STP-2 plasma is several percent of the electron density.

3.3 Origin and Behavior of Impurity

In the STP-2 plasma the dominant impurity has been found to be oxygen, and several carbon lines have been also observed. For the following reasons we assume that these impurities come from the discharge tube wall. The purity of the deuterium gas including hydrogen is about 99.99 % in this experiment, and the density of oxygen has been found to be several percent of the electron density. Therefore, it is obvious that the impurity does not come from the working gas. On the other hand, the discharge tube has been made of quartz for the fast discharge experiment, and baking out and discharge clearing could be made only to a limited extent. The basis pressure was about 5×10^{-7} torr, which was much poor compared with that of tokamaks. Thus, a high level of gas atoms and molecules may have been contained on the wall surface. Break-down of the θ-pinch discharge has occurred along the wall surface and the STP-2 had no limiter. In fact, streak-photograph indicates that a strong plasma emission is observed in the periphery region at the beginning of the discharge. This suggests that a strong plasma-wall interaction takes place in the initial phase of the discharge.

Figure 13 shows the spatial distribution of OII line at 2 and 4 μsec. At 2 μsec n_e has been found to have a rather smooth distribution

with a slight maximum at the tube center. From the discussion in Sec. 3.2 and n_e and T_e in Fig.5, it is expected that the dominant ionization stage of oxygen is OII at these early times. Thus, it may well be expected that the emission line intensity of Fig.13 gives a good measure of the impurity oxygen density. It is clearly seen that the impurity is concentrated near the tube wall at 2 μsec, and that it moves inward later. This confirms our earlier assumption about the origin of the impurity. The situation should be almost the same for carbon.

The dominant ion of oxygen is OIII after 4 μsec and Figure 14 shows the population density profile of OIII ($2p3p(^3D)$) for 4 to 10 μsec. It is noted that the decrease with time in the population density is attributed to the decrease in the electron temperature. Comparison with Figs.5 and 14 indicate that oxygen ions move following the deuterium main plasma. This behavior of impurity seems quite reasonable when we consider the collision frequency of oxygen and deuterium ions; the electron density is high and temperature is low so that the collision frequency is high enough ($\sim 10^6$ Hz) to couple to the motion of the impurity with the plasma. This conclusion suggests that the radiation loss by impurities is very large in the central part of the plasma. In contrast to tokamak plasmas the overall energy confinement time of the STP-2 plasma is largely affected by the radiation loss of oxygen in the high density part of the plasma. This conclusion also verifies the conventional assumption in the computer simulation [8] for energy balances that impurity particles move with a plasma.

4. DISCUSSION AND CONCLUSION

The impurity oxygen OII and OIII have been assumed to be in the

ionizing-state in our analysis in Sec.3.2. Its validity is examined on the basis of the approximation of hydrogenic ion. In the collisional radiative model the population density of excited-state p is given as a sum of the two terms [16]:

$$n(p) = Z(p)\cdot\gamma_0(p)\cdot n_z\cdot n_e + \frac{Z(p)}{Z(1)}\cdot\gamma_1(p)\cdot n(1) \ , \tag{6}$$

with

$$Z(p) = \frac{g(p)}{2\omega_z}\cdot\left(\frac{h^2}{2\pi m T_e}\right)^{3/2}\cdot\exp\left(\frac{\chi(p)}{T_e}\right) \ . \tag{7}$$

Here, the notations are as follows:

n_z : density of the fully stripped Z-charged ion,

$\chi(p)$: ionization potential from level p,

$g(p)$: statistical weight of level p,

ω_z : partition function of the Z-charged ion,

h : Planck's constant.

The quasi-steady-state solution $\gamma_0(p)$ and $\gamma_1(p)$ are called the population coefficients and are functions of electron density and temperature [27]. The first term in Eq.(6) represents the contribution from Z-charged ion and the second term represents that from the ground state of (Z-1)-charged hydrogenic ion. In evaluating the two terms it is convenient to employ the scaling law for n_e and T_e; effective density n_e^* and temperature T_e^* [26] are given by

$$n_e^* = \frac{n_e}{z^7} \ , \tag{8}$$

$$T_e^* = \frac{T_e}{z^2} \ . \tag{9}$$

The electron density and temperature are 10^{15} cm^{-3} and 10 eV at 5 μsec.

The ratio $n(1)/n_z$ is given from Fig. 11 and Fig. 12 for OII, and OIV density is estimated from the ionization time given in Fig.(8) to lead to $n(1)/n_z$ for OIII. The first and second terms in Eq.(6) are calculated by using these parameters and tabulated values [27] of $\gamma_0(p)$ and $\gamma_1(p)$ for (Z-1)-charged ion. For OII (Z = 2) and OIII (Z = 3) the second term is found to be about 10 to 20 times as large as the first. However, if the electron temperature becomes lower than 5 eV for the later periods the first is comparable to the second. Therefore, the plasma is considered to be in the ionizing-state at 5 μsec and it is consistent with Eqs.(3) and (4). It should be noted that OIII ions remain the dominant ionization stage for the later periods because the recombination time for OIII is about one hundred microsecond even if high electron density effect is included [28].

The radiation trapping has not been considered because all of the measured lines are in the visible and quartz-violet region. If, on the other hand, measurements were performed in the vacuum-ultraviolet region and the lines were correlated with the ground states, the radiation trapping would have to be taken into account especially for plasma with high impurity density like the STP-2 in this case, however, the population density would be evaluated simply by using the corona model. Therefore, the analysis would be free from the complicated relations between the high-lying levels as described by Eqs.(3) and (4).

The conclusion: in the STP-2 plasma the origin of the impurity is the wall of the discharge tube, and its density is about several percent of the electron density. Since the radiation loss power of oxygen as estimated in ref.[29] is almost equal to the ohmic heating power, the energy confinement is completely determined by ionization and radiation losses of impurities. This conclusion is consistent with the rapid

decrease in the electron temperature in Fig.6. A comprehensive study of energy balance in the STP-2 is in progress by using a two dimensional MHD code [30] where the ionization and radiation losses due to impurity and neutral hydrogen are included in the solution of the MHD equations.

Acknowledgements

The author is grateful to Professor K. Hirano for his interest and encouragements throughout this study. Useful discussions and suggestions covering atomic physics by Dr. T. Fujimoto and Dr. T. Kato are acknowledged. He thanks Professors T. Amano and K. Mori for helpful discussions and thanks all members of the high beta group in the Institute for their cooperations.

REFERENCES

[1] KRAUSE, H., Verh. Deut. Phys. Ges. 7 (1972) 452.

[2] HIRANO, K., OHI, M., KITAGAWA, S., and HAMADA, Y., Proc. 2nd Topical Conf. Pulsed High-Beta Plasmas, F5/209 (1972).

[3] OEPTS, D., LISTER, G.G., LONG, J.W., VAN DER MEER, A.F.G., OOMEN, A.A.M. and BOBELDIJIK, C., in Controlled Fusion and Plasma Physics (Proc. 9th Europ. Conf., Oxford, 1979) 1 (1979) 105.

[4] Proc. the Finite Beta Workshop (ed., Coppi, B and Sadowski, W.) Varenna (1977).

[5] D'LPPOLITE, D.A., FREIDBERG, J.P., and REM, J., Phys. Fluids 21 (1978) 1600.

[6] YAMAGUCHI, S., NAGATA, A., and HIRANO, K., to be published.

[7] COS, D.P., and TUCKER, W.H., Astrophys. J. 157 (1969) 1157.

[8] BECKER, G., GRUBER, O., KRAUSE, H., MAST, F., and WILHELM, R., Nucl. Fusion 18 (1978) 1653.

[9] NAGATA, A., YAMAGUCHI, S., HIRANO, K., Jpn. J. Appl. Phys. 20 (1981) 151.

[10] YAMAGUCHI, S., and WU, CH., to be published.

[11] FACOM Scientific Subroutine Library 2 (1978) 162.

[12] YASUTOMO, Y., MIYATA, K., HIMENO, SH., ENOTO, T. and OZAWA, Y., Plasma Sci. 9 March (1981) 18.

[13] BARR, W.L., J. Opt. Soc. Am. 52 (1962) 885.

[14] TFR GROUP, Nucl. Fusion 20 (1980) 885.

[15] LOTZ, W., IPP 1/62 (1967).

[16] FUJIMOTO, T., J. Phys. Soc. Japan 47 (1979) 265.

[17] FUJIMOTO, T., J. Phys. Soc. Japan 47 (1979) 273.

[18] BATES, D.R., KINGSTONE, A.E., and MCWHIRTER, R.W.P., Proc. R. Soc. 267 (1962) 297.

[19] BATES, D.R., and KINGSTONE, A.E., Planet. Space Sci. 11 (1963) 1.

[20] MCWHIRTER, R.W.P. and HEARN, A.G., Proc. Phys. Soc. 82 (1963) 641.

[21] KATO, T., IPPJ-AM-4 (1978).

[22] WIESE, W.L., SMITH, M.W., and GLENNON, B.M., "Atomic Transition Probabilities", NSRDS-NBS4, National Bureau of Standards, Washington, D.C. 20402 (1966).

[23] DOSCHEK, G.A., FELDMAN, U., BHATIA, A.K., and MASON, H.E., Astrophys. J. 226 (1978) 1129.

[24] BHATIA, A.K., DOSCHEK, G.A., and FELDMAN, U., Astron. Astrophys. 76 (1979) 359.

[25] MANDELBERG, H.I., Phys. Rev. A 2 (1970) 1372.

[26] FUJIMOTO, T., KAKUYUGO KENKYU Supple (1981) (Japanese).

[27] FUJIMOTO, T., SUGIYAMA, I. and FUKUDA, K., Mem. Fac. Eng. Kyoto Univ. 34 (1972) 249.

[28] FUJIMOTO, T., J. Phys. Soc. Japan 49 (1980) 1561.

[29] HAYAKAWA, S., and KATO, T., JAERI-M8060 (1979).

[30] NAGATA, A. et al., to be published.

FIGURE CAPTIONS

Fig.1 Schematic drawing of the STP-2 and diagnostics apparatus around the torus.

Fig.2 Waveforms of plasma current and toroidal field intensity.

Fig.3 The spectroscopic system and its setting for the torus of the STP-2.

Fig.4 Profiles of the electron density and temperature at 5 μsec obtained by a ruby laser scattering.

Fig.5 Temporal evolution of the spatial profile of the electron density from 4 to 10 μsec.

Fig.6 Time history of the electron density and temperature in the center of the discharge tube.

Fig.7 Temporal evaluation of oxygen spectrum lines; numbers 1, 2 and 3 represent the lines of OI (6158 Å), OII (4076 Å) and OIII (3760 Å), respectively.

Fig.8 Diagram of ionization potentials and times for oxygen ion; τ_o is the ionization time by Lotz's coefficient in the condition of T_e and n_e being 10 eV and 10^{15} cm^{-3}, τ^* is the effective value in the same condition. The dotted lines show effective levels of ionization potential depended on "ladder-like excitation-ionization" [16].

Fig.9 Density profiles of OII ($2p^2 3d(^4F)$) and OIII ($2p3p(^3D)$) at 5 μsec obtained by using the cylindrically asymmetric Abel inversion. Error of the profiles is about 20 to 30 %.

Fig.10 Partial energy diagram of OIII triplet series. In considering the rate equations for 2p3s and 2p3p, the solid lines indicate the transitions by electron impact and the wavy lines mean radiation decaies.

Fig.11 The population density profile of OIII ground state at 5 μsec obtained from the solutions of the rate equations. Error bar is calculated from the error of the electron density. The dotted line shows the population density in triplet series and the solid line means the sum of triplet, singlet and quintet levels of the ground state densities.

Fig.12 Population density profile of OII quartet series at 5 μsec. Error bar depends on the error of the electron density.

Fig.13 Spatial distribution of OII (4076 Å) and $2p^2 3d(^4F)$ at 2 and 4 μsec. The thick line shows line intensity and the slender line the population density.

Fig.14 Temporal evolution of the spatial profile of OIII ($2p3p(^3D)$) ion density from 4 to 10 μsec.

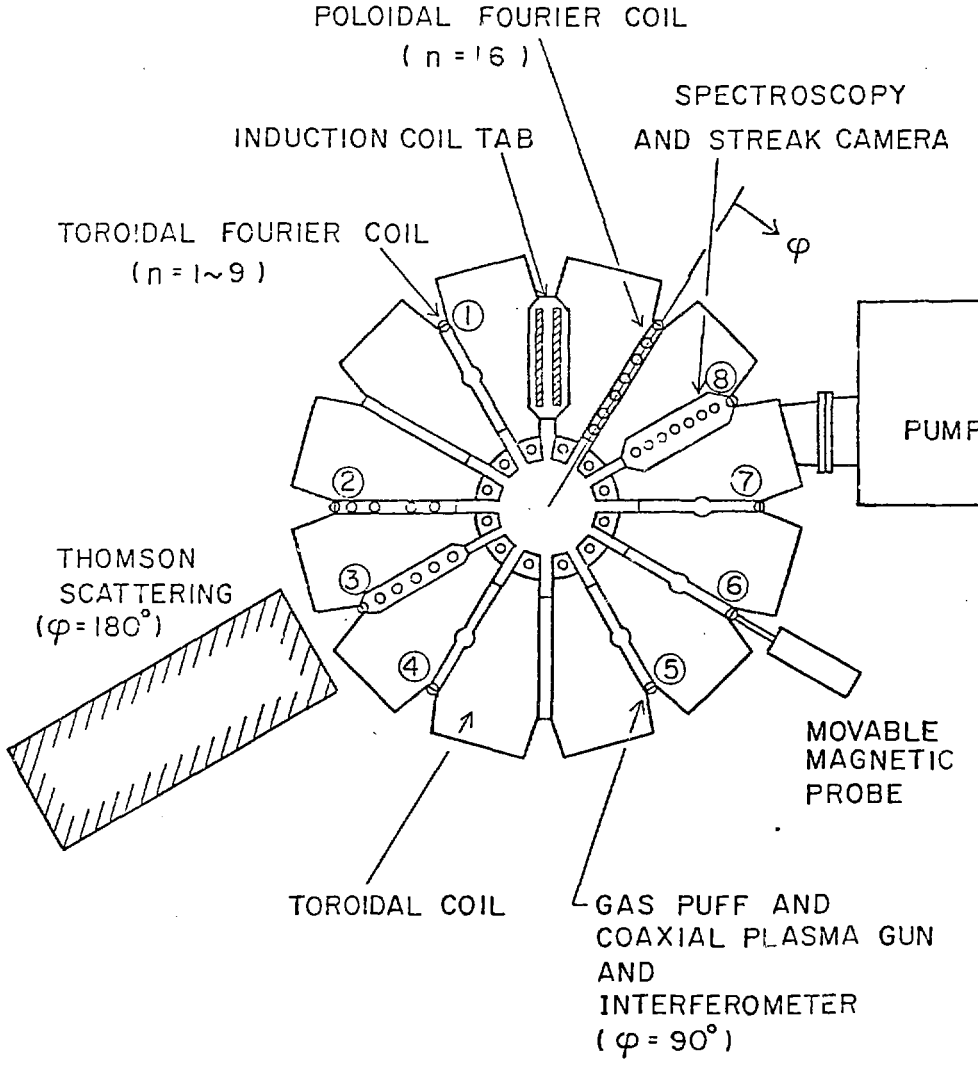
POLOIDAL FOURIER COIL
(n = 16)
SPECTROSCOPY
AND STREAK CAMERA
INDUCTION COIL TAB
TOROIDAL FOURIER COIL
(n = 1~9)
φ
PUMP
THOMSON
SCATTERING
(φ = 180°)
MOVABLE
MAGNETIC
PROBE
TOROIDAL COIL
GAS PUFF AND
COAXIAL PLASMA GUN
AND
INTERFEROMETER
(φ = 90°)

Fig. 1

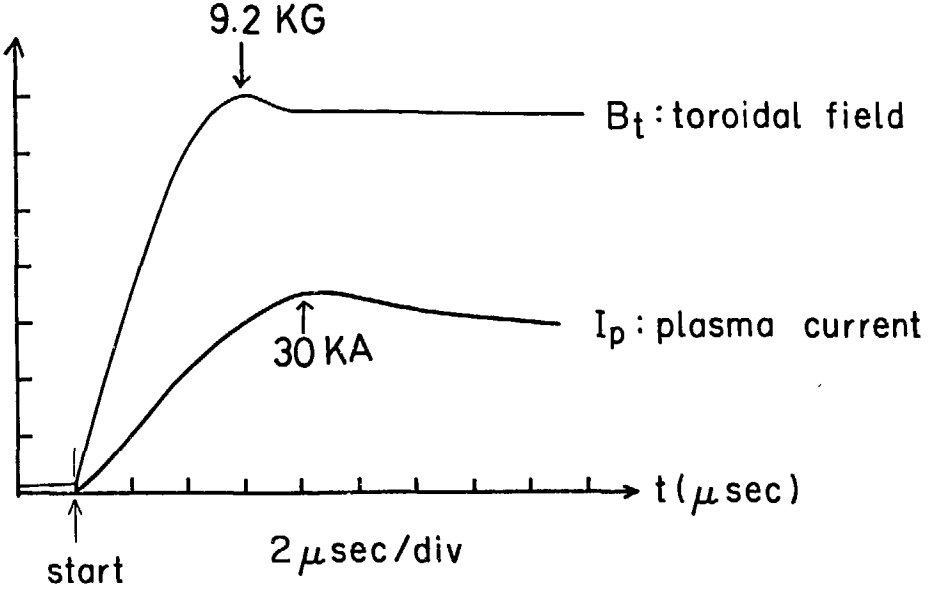
9.2 KG
B_t : toroidal field
I_p : plasma current
30 KA
t (μ sec)
start
2 μ sec / div

Fig. 2

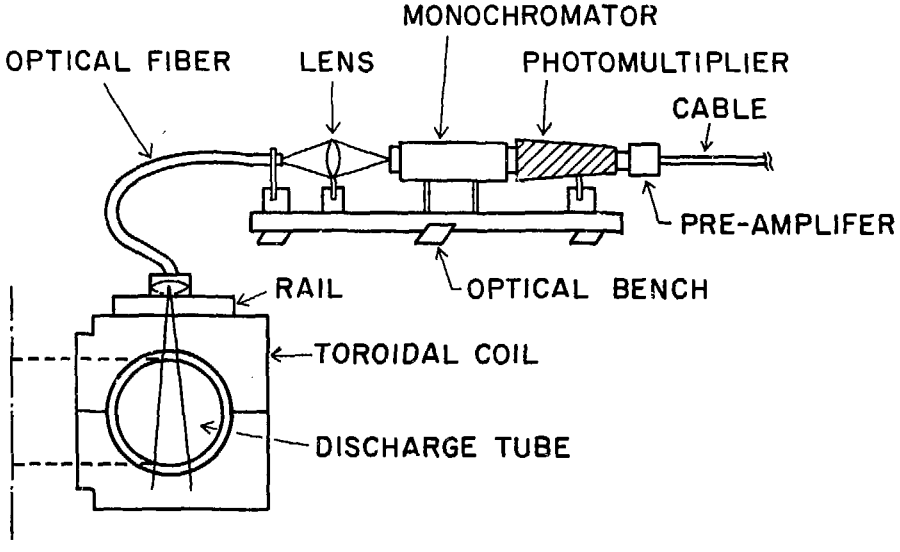
MONOCHROMATOR
OPTICAL FIBER
LENS
PHOTOMULTIPLIER
CABLE
PRE-AMPLIFER
RAIL
OPTICAL BENCH
TOROIDAL COIL
DISCHARGE TUBE

Fig. 3

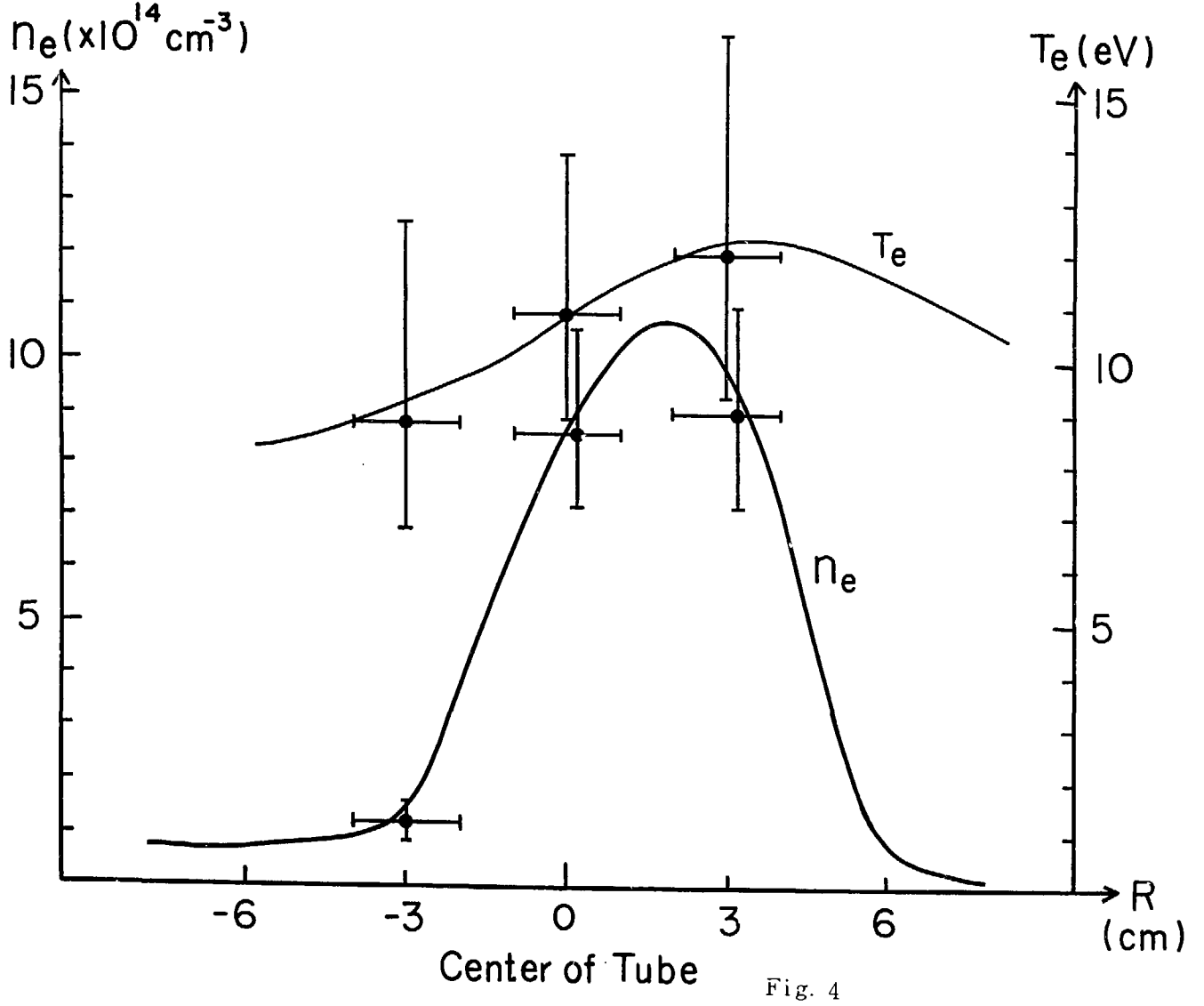
$n_e(\times 10^{14} cm^{-3})$
15
10
5
$T_e(eV)$
15
10
5
T_e
n_e
-6
-3
0
3
6
R
(cm)
Center of Tube

Fig. 4

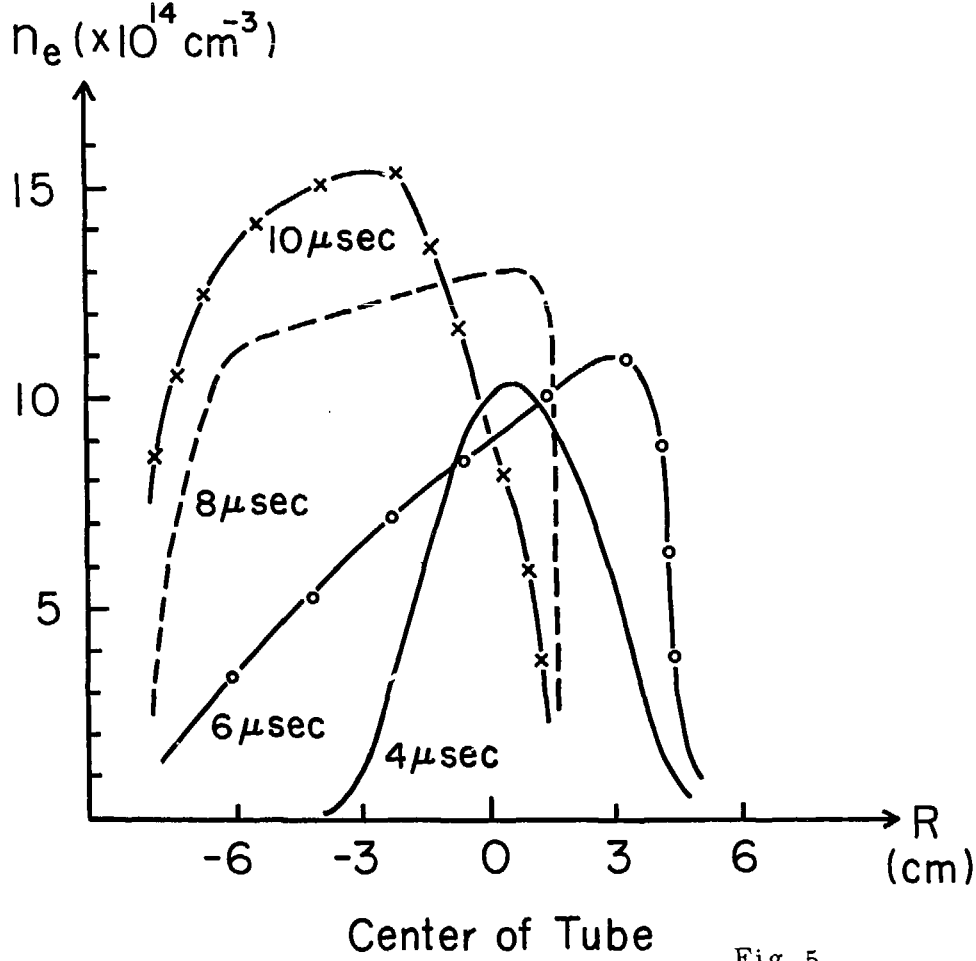
n_e ($\times 10^{14}$ cm^{-3})
15
10
5
10μsec
8μsec
6μsec
4μsec
-6
-3
0
3
6
R
(cm)
Center of Tube

Fig. 5

Fig. 6

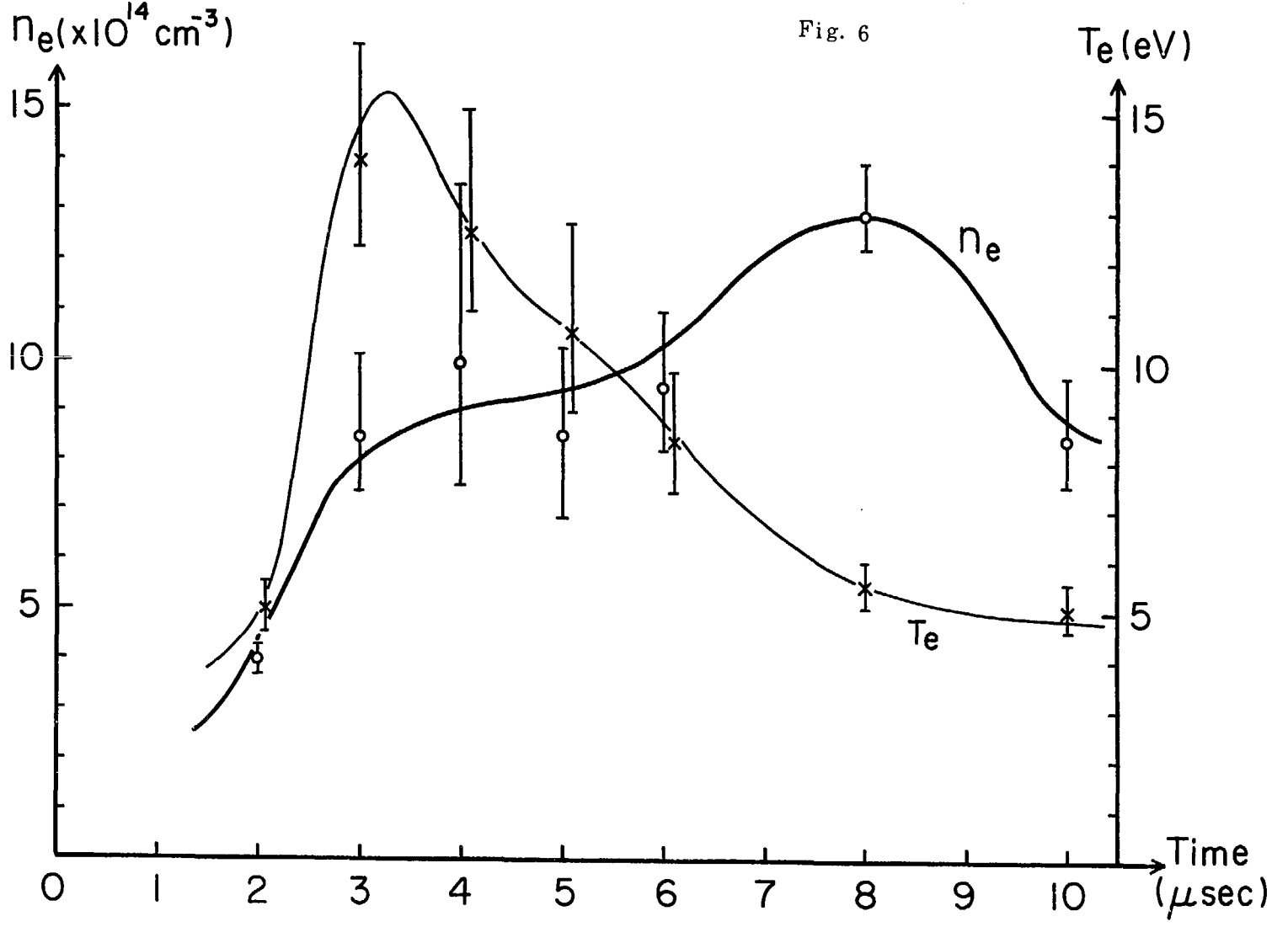

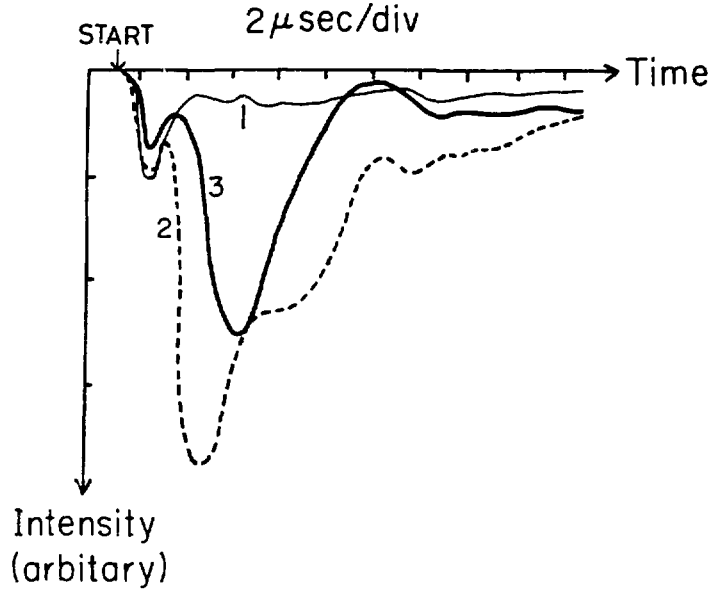

Fig. 7

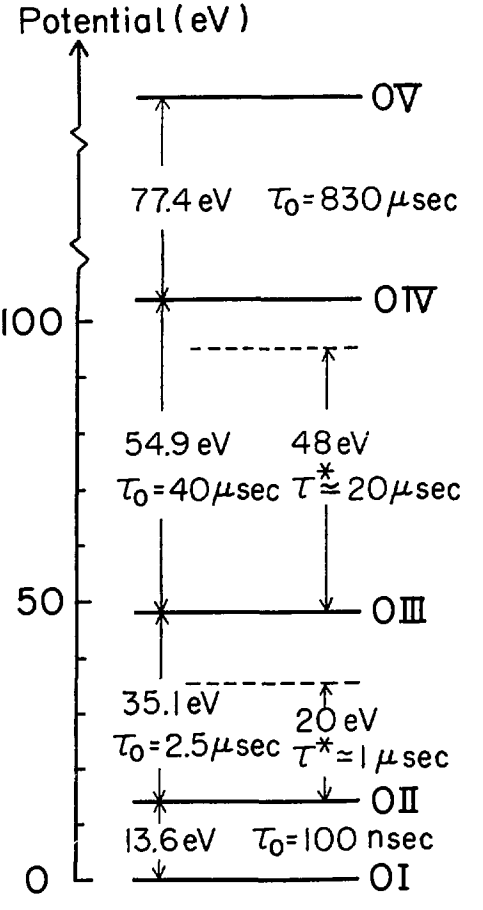
Potential (eV)
100
50
0
OV
77.4 eV
τ_0=830 μsec
OIV
54.9 eV
τ_0=40 μsec
48 eV
$\tau^* \simeq$ 20 μsec
OIII
35.1 eV
τ_0=2.5 μsec
20 eV
$\tau^* \simeq$ 1 μsec
OII
13.6 eV
τ_0=100 nsec
OI

Fig. 8

Fig. 9

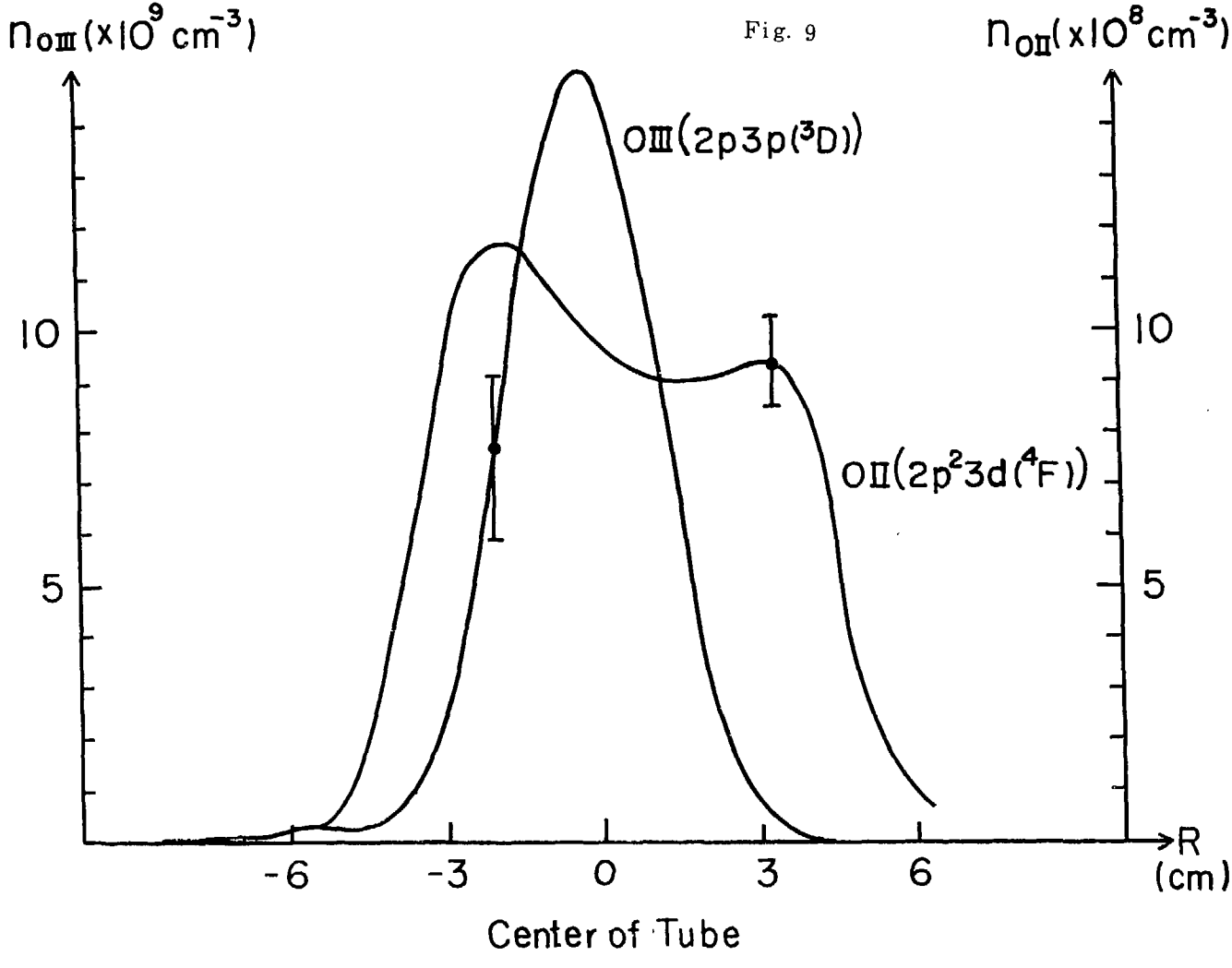
$n_{OIII}(\times 10^{9}\,cm^{-3})$
$n_{OII}(\times 10^{8}\,cm^{-3})$
OIII(2p3p(3D))
OII(2p23d(4F))
10
5
10
5
-6
-3
0
3
6
R
(cm)
Center of Tube

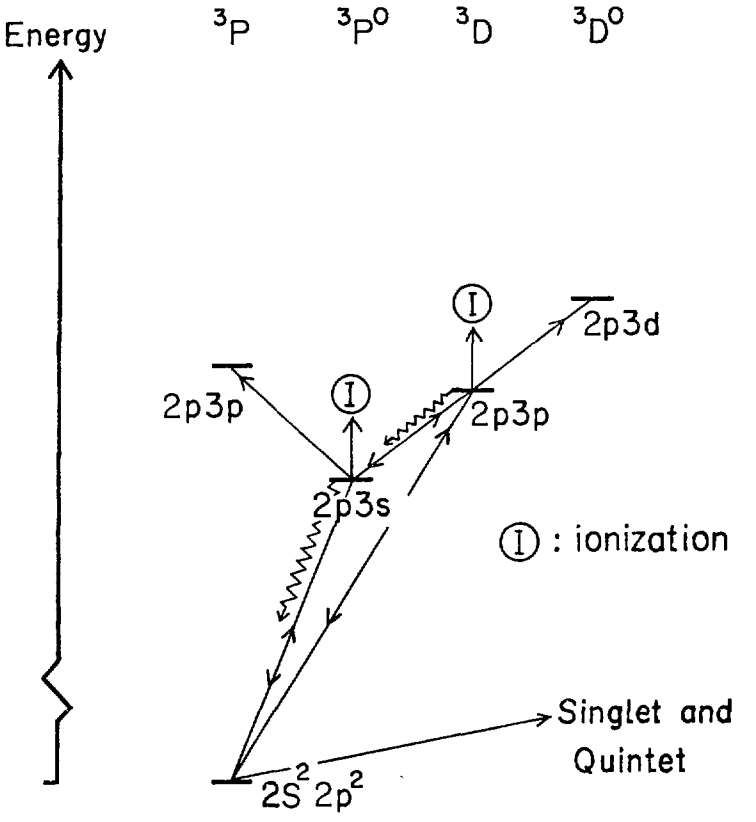
Energy
^3P
$^3P^o$
^3D
$^3D^o$
2p3d
2p3p
2p3p
2p3s
Ⓘ : ionization
Singlet and
Quintet
$2S^2 2p^2$

Fig. 10

Fig. 11

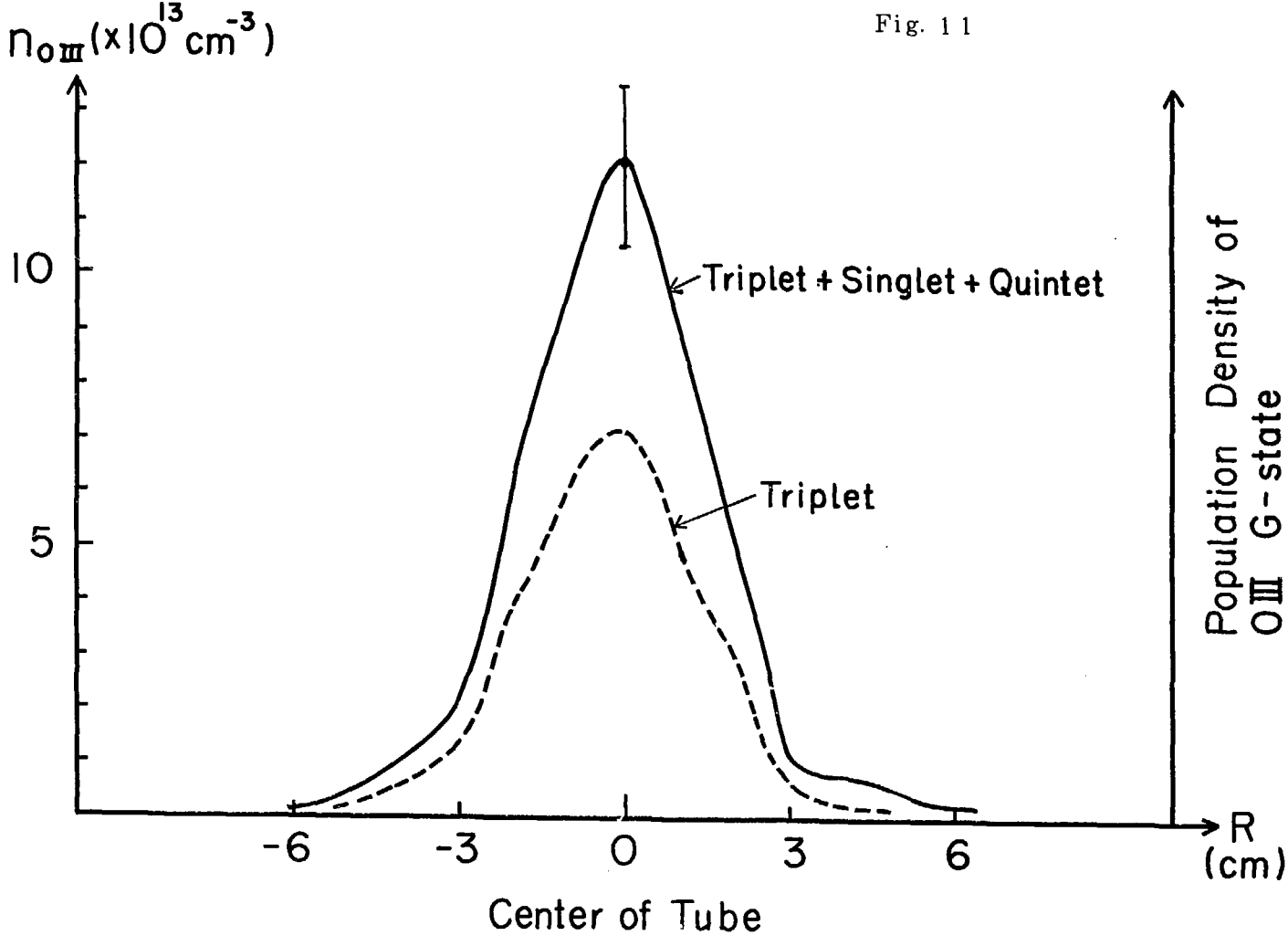
$n_{OIII}(\times 10^{13} cm^{-3})$
10
5
Triplet + Singlet + Quintet
Triplet
Population Density of OIII G-state
-6
-3
0
3
6
R (cm)
Center of Tube

Fig. 12

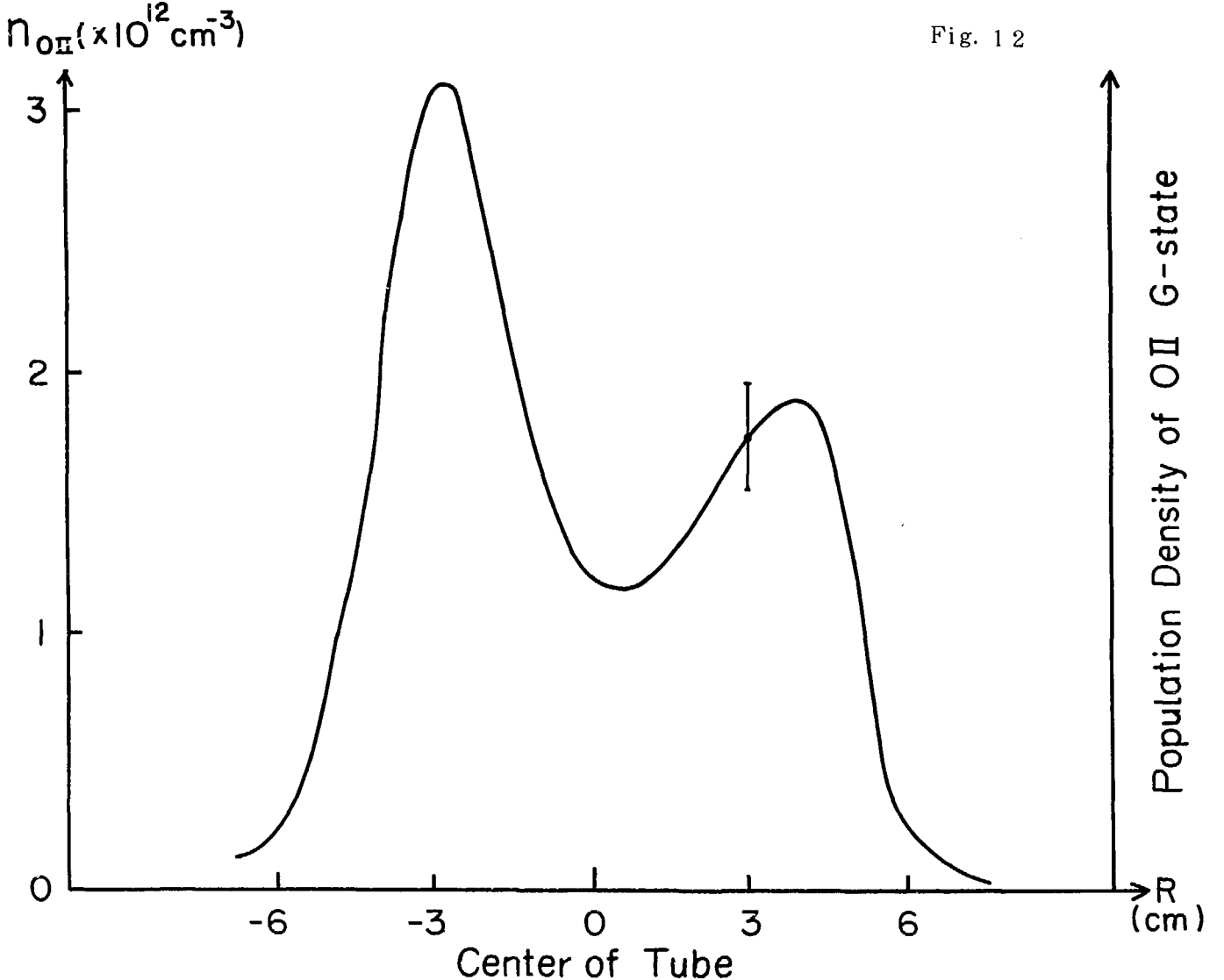
$n_{OII}(\times 10^{12} cm^{-3})$
3
2
1
0
-6
-3
0
3
6
R
(cm)
Center of Tube
Population Density of OII G-state

Fig. 13

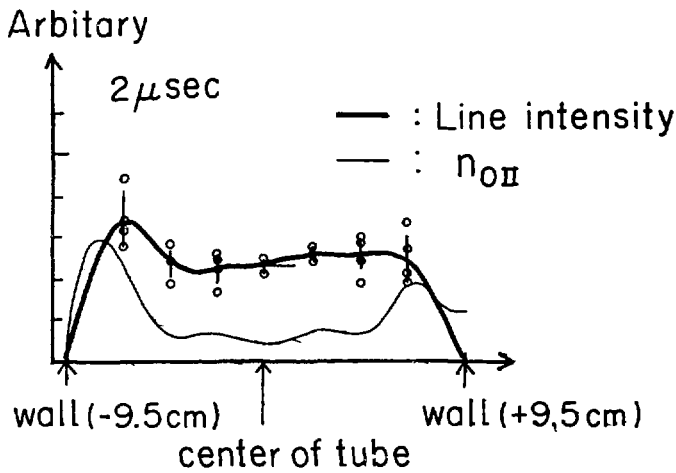
Arbitary
2μsec
: Line intensity
: n_{OII}
wall (-9.5cm)
wall (+9,5cm)
center of tube

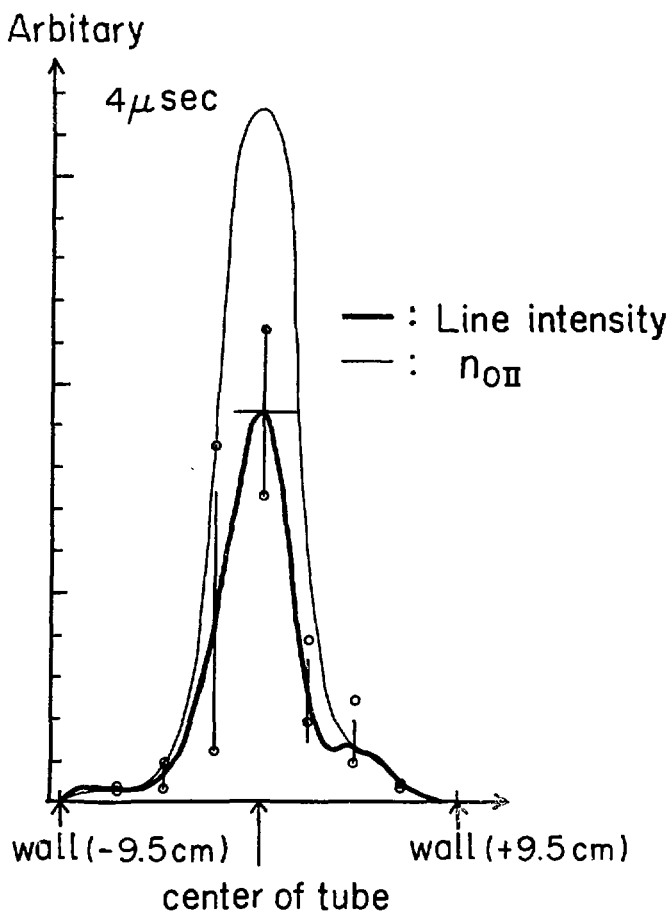
Arbitary
4μsec
: Line intensity
: n_{OII}
wall (-9.5cm)
wall (+9.5cm)
center of tube

Fig. 14

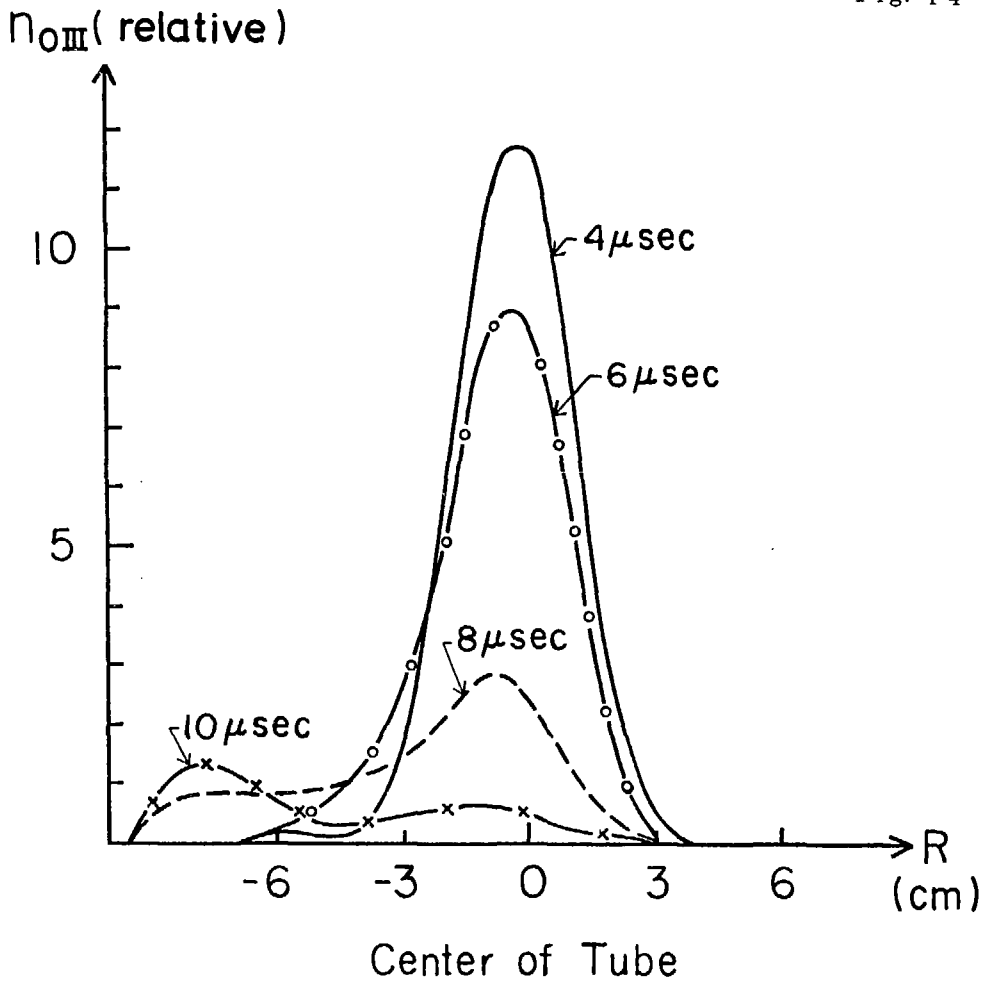
n_{OIII}(relative)
10
5
4μsec
6μsec
8μsec
10μsec
-6
-3
0
3
6
R
(cm)
Center of Tube